

# Topological inverse band theory in waveguide quantum electrodynamics

Yongguan Ke<sup>1,2,3</sup>, Jiakuan Huang<sup>2</sup>, Wenjie Liu<sup>2,3</sup>, Yuri Kivshar<sup>4,\*</sup> and Chaohong Lee<sup>1,2,3†</sup>

<sup>1</sup>College of Physics and Optoelectronic Engineering, Shenzhen University, Shenzhen 518060, China

<sup>2</sup>Guangdong Provincial Key Laboratory of Quantum Metrology and Sensing & School of Physics and Astronomy, Sun Yat-Sen University (Zhuhai Campus), Zhuhai 519082, China

<sup>3</sup>State Key Laboratory of Optoelectronic Materials and Technologies,

Sun Yat-Sen University (Guangzhou Campus), Guangzhou 510275, China and

<sup>4</sup>Nonlinear Physics Center, Research School of Physics,

Australian National University, Canberra, Australian Capital Territory, Australia.

(Dated: January 16, 2023)

Topological phases play a crucial role in both fundamental physics of light-matter interaction and emerging quantum technologies. However, due to photonic scattering the topological band theory of waveguide QED systems is known to break down, because the energy bands become divergent and disconnected. Here, we introduce a concept of the inverse energy band and explore analytically the topological scattering in a waveguide with an array of quantum emitters. We uncover a rich structure of topological phase transitions, symmetric scale-free localization, completely flat bands, and the corresponding dark Wannier states. While bulk-edge correspondence is broken, the Zak phase of inverse energy band can be extracted via long-time average of mean cell position in quantum walks. Surprisingly, the winding number of the scattering textures depends on both the topological phase of inverse subradiant band and the oddity of the cell number. Our work opens a novel field of the topological inverse bands, and it brings a fundamental vision on topological phases in light-matter interactions.

## INTRODUCTION

Light-matter interaction plays a crucial role in the fundamental sciences [1, 2], and it underpins the rapid progress of quantum technologies. Understanding intrinsic mechanisms of absorption as well as spontaneous and stimulated emissions leads to the development of practical applications such as solar cells, LEDs, and lasers [3]. Introducing topology into light-matter interaction could bring new advances such as topological lasers [4–7], in which monochromaticity, efficiency, and emission stability become superior to those observed for conventional lasers. To unleash the power of topology in light-matter interaction [8], it is important to understand the role of topological phases at the microscopic level of quantum electrodynamics (QED).

Waveguide QED studies photons propagating in waveguides, excitation of quantum emitters, and strong interaction between them [9–12], providing an excellent platform to explore the interplay between topology and light-matter-interaction [13–26]. We notice that the previous studies are based on the well-established topological band theory allowing to calculate topological phases and topological invariants [27, 28]. However, due to infinite-range coupling, in waveguide QED the energy band splits into two disconnected polariton branches [29], which hinders the straightforward application of the topological band theory. Up to now, it is still unclear how the bulk topological phase or topological invariant are imprinted in photonic scattering.

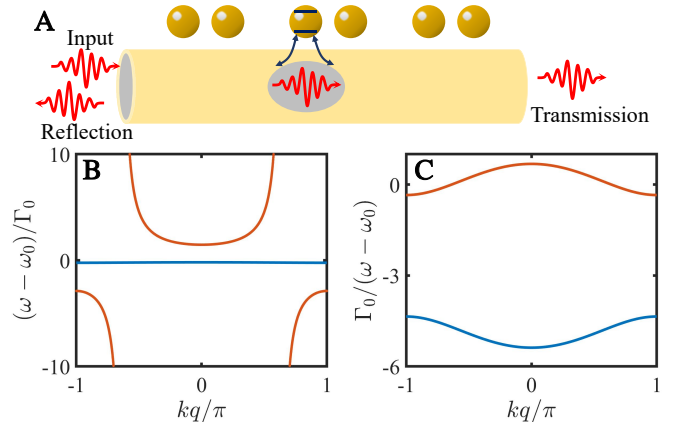


FIG. 1. Schematic diagram of photonic scattering and inverse energy band. **A** Diagram of photon in a waveguide scattered by quantum emitters. The emitter positions are arranged as  $z_j = d[j + \delta \cos(\pi j + \theta)]$  with the averaged spacing  $d$ , the modulation strength  $\delta$ , and the modulation phase  $\theta$ . **B** Energy band. **C** Inverse energy band. The parameters are chosen as  $\delta = 0.4$ ,  $\theta = 0$  and  $\varphi = 1$ .

Here, we suggest and implement the topological inverse energy band theory based on a proof-of-principle waveguide QED with inversion symmetry, as depicted in Fig. 1, and we uncover a connection between topological phases and photonic scattering. We find *analytically* unexpected rich topological phase transitions driven by the spatial structure and resonant frequency of emitters. We also obtain *analytically* the resonant frequencies that favor a completely flat band and a group of dark Wannier states equally occupying two emitters. Due to a breakdown of the bulk-edge correspondence, we propose to measure the Zak phase of the inverse energy band via

\* Corresponding author. Email: yuri.kivshar@anu.edu.au

† Corresponding author. Email: chleeen@szu.edu.cn; chleeen@gmail.com

the long-time averaging the mean cell position in quantum walks. We use the reflection and transmission coefficients to construct scattering textures, which are winding as the photonic frequency is swept along an inverse subradiant band. Importantly, the winding number of scattering depends on both the topological phase of the inverse band and oddity of the cell number. We believe our work opens a field of topological inverse band theory, it provides new insights into the role of topological phases imprinted in light-matter interaction, and it paves a way to engineer the dark states for quantum information storage and precision frequency measurements.

## RESULTS

### Topological waveguide QED with inversion symmetry

As a proof-of-principle example, we consider an array of quantum emitters in a photonic waveguide. The quantum emitters are two-level systems with resonant frequency  $\omega_0$  and positions arranged as  $z_j = d[j + \delta \cos(2\pi/qj + \theta)]$ ; see Fig. 1 A. Here, each unit cell contains  $q = 2$  emitters,  $d$  is the spacing constant,  $\delta$  and  $\theta$  are respectively the modulation strength and phase. The basic process is that the photon is absorbed by emitters and is transferred into an excitation, which can be reversely transferred into a photon. The motion of an excitation is described by an effective Hamiltonian [30] (see Supplementary Materials for details),

$$H_{eff} = \sum_{j=1}^{2N} \hbar\omega_0 b_j^\dagger b_j - i\hbar\Gamma_0 \sum_{j,l=1}^{2N} b_j^\dagger b_l e^{i\varphi|z_l - z_j|/d}. \quad (1)$$

Here,  $N$  is the number of cells and the scaled Planck constant  $\hbar$  is set as a unit in the following.  $\Gamma_0 = g^2/c$  is the radiative decay rate of a single emitter with  $g$  denoting the coupling strength between excitation and photon and  $c$  being the velocity of light. The hopping of excitation from any two emitters is assisted by emission and reabsorption a photon in the waveguide. The hopping strength is an infinite range with a phase shift, in which phase unit  $\varphi = \omega d/c$  depends on the injected photonic frequency  $\omega$ . When the spacing constant is small enough, one may take the Markov approximation by replacing the phase constant with  $\varphi = \omega_0 d/c$  [30].

By applying Bloch theorem, we can immediately obtain Hamiltonian in momentum space  $H_k$  and the Bloch states  $|\psi_{n,k}\rangle = \sum_{j,l} e^{ikqj} u_{n,k}(l) |qj + l\rangle$  with energy  $\omega_{n,k}$  (see Methods). We find that the energy band is diverged at  $k = \pm\varphi$  and is split into upper and lower polariton branches; see Fig. 1 B. The divergence of the energy band originates from the photonic scattering and hinders the application of topological band theory. To avoid the divergence, we define inverse energy band as

$$\bar{\omega}_k = (\omega_k - \omega_0)^{-1}, \quad (2)$$

which can be obtained by solving  $(H_k - \omega_0 I)^{-1} |\bar{u}_{n,k}\rangle = \bar{\omega}_{n,k} |\bar{u}_{n,k}\rangle$  with identity operator  $I$ . The inverse energy band glues the upper and lower polariton branches and becomes a continuous function; see Fig. 1 C. By fixing the disconnection problem, we can easily define topological phases and topological invariants based on the inverse band as usual. Although the Hamiltonian and its inversion share the same eigenstates, they have different band indices and thus the inverse energy band may uncover novel topological states which are failed to be found by the original energy band.

### Topological phase transition and dark Wannier states

Since the effective Hamiltonian has the inversion symmetry  $H(i, j) = H(2N + 1 - i, 2N + 1 - j)$ , we can define the Zak phase of the  $n$ th inverse band as

$$\gamma = i \int_{-\pi/2}^{+\pi/2} \langle \bar{u}_{n,k} | \frac{\partial}{\partial k} | \bar{u}_{n,k} \rangle dk. \quad (3)$$

Fig. 2 A shows the Zak phase as a function of the modulation phase and the hopping phase constant. Surprisingly, the topological phase diagram is unexpected rich, with nontrivial phase  $\gamma = \pi$  for yellow regions and trivial phase  $\gamma = 0$  for white regions. The red lines and the black dashed lines mark the topological phase boundaries, and the parameters for flat band with energy  $\omega = \omega_0$ , which have been analytically obtained in the Methods. When a flat band with energy  $\omega = \omega_0$  exists, we have to combine energy band and inverse energy band to extract the topological phase. For a fixed spatial structure, we can drive the topological phase transition by the resonant frequency ( $\varphi = \omega_0/cd$ ), which can be controlled by either the resonant frequency of injected photon or the Zeeman shift induced by magnetic field. This is in stark contrast to the topological phases in electronic materials which are largely determined by the crystal structure.

To explore the bulk-edge correspondence, we calculate the inverse participation ratio of eigenstates under the open boundary conditions,  $\text{IPR} = \sum |\psi_n(j)|^4$ . Fig. 2 B shows the dependence of IPRs on the hopping phase constant and the inverse energy. There are no edge modes in the inverse band gaps, indicating the breakdown of the bulk-edge correspondence. However, symmetric scale-free localized states (Fig. 2 C),  $|\psi_j|^2 \sim (e^{-\alpha j/N} + e^{\alpha j/N})^2$ , exist in the continuous spectrum with larger IPRs. These results can be explained by an inverse of the effective Hamiltonian, which turns out to be an Su–Schrieffer–Heeger (SSH) model with effective radiative defects at the boundaries; see Supplementary Materials for details. The emergent nontrivial SSH model comes from the inversion symmetry in the conversion between trivial excitation and photon. This is in stark contrast to previous works which rely on the existing topological phases of either the photon subspace [14, 23] or excitation subspace [15, 22].

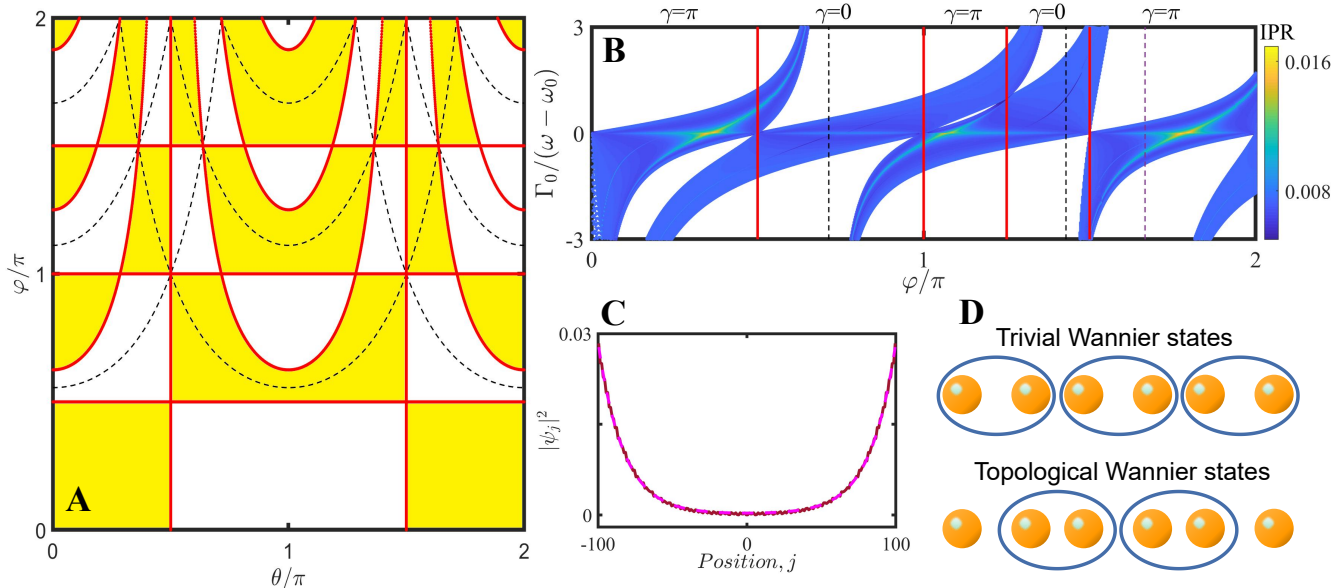


FIG. 2. Topological phase transition, breakdown of bulk-edge correspondence and topological flat band. **A** Topological phase diagram. Dashed black lines denote the positions of flat bands. The number of cells is  $N = 100$ . **B** The inverse participation ratio under open boundary conditions. The number of cells is  $N = 100$ . **C** Symmetric scale-free localized states with the largest IPR (green solid line), and the fitting function  $|\psi_j|^2 \sim (e^{-\alpha j/N} + e^{\alpha j/N})^2$  (cyan dashed line). The other parameters are chosen as  $\theta = \pi/3$  and  $\varphi = 2\pi/3$ . **D** Schematic diagram of Wannier states for the topologically trivial and nontrivial flat bands. There are  $N(N-1)$  Wannier states which are symmetric inter (intra)-cell superposition for trivial (topological) flat-band systems with  $N$  cells. The above calculations are performed with modulation strength  $\delta = 0.4$

A stark difference between the trivial and topological nontrivial phases is the number ( $S$ ) of subradiant states in the lower inverse band, i.e.,  $S = N$  for a trivial phase and  $S = N - 1$  for a topological nontrivial phase. The subradiant states in the lower inverse band become dark states when the band becomes complete flat with energy  $\omega = \omega_0$  (see Supplementary Materials for details). Because the flat band has zero group velocity and infinite effective mass, the lifetime of excitation can be infinitely long. We can construct dark Wannier states of the flat band around the  $R$ th-cell as,

$$|w_{n,R}\rangle = \frac{1}{\sqrt{N}} \sum_k e^{-ikqR} |\psi_{n,k}\rangle, \quad (4)$$

which are simply given by inter-cell superposition  $(|2j-1\rangle + |2j\rangle)/\sqrt{2}$  ( $j = 1, 2, \dots, N$ ) in the trivial phase and intra-cell superposition  $(|2j\rangle + |2j+1\rangle)/\sqrt{2}$  ( $j = 1, 2, \dots, N-1$ ) in the topological nontrivial phase; see Fig. 2 **D**. These dark Wannier states form a decoherence-free subspace, which is simple, arranged in order, and with the same energy of resonant frequency  $\omega_0$ . These features could potentially be used for quantum memory and quantum information process.

### Extraction of topological phase via quantum walks

Since edge state is no longer an evidence for topological phase, below we show how to extract the topological phase from the short-time dynamics of an excitation. The effective Hamiltonian for excitation has inversion symmetry and break chiral symmetry due to the long-range couplings. Adopted the dynamical scheme in Refs. [31, 32], we propose to prepare an excitation in the  $N$ th emitter and observe the time average of the mean cell position of excitation undergoing quantum walks,

$$\bar{P}(T) = \frac{1}{T} \int_0^T \sum_{j=1}^N j (|\psi(2j-1, t)|^2 + |\psi(2j, t)|^2) dt. \quad (5)$$

The Zak phase is related to a winding number,  $\mathcal{M}$ , and hence the mean cell position,

$$\gamma = \mathcal{W}\pi = -2\pi \lim_{T \rightarrow \infty} \bar{P}(T). \quad (6)$$

However, in our system, we have to compromise that the time should be less than the lifetime of excitation and large enough for the topological phase to take effect. Given  $\delta = 0.4$ ,  $\theta = \pi/3$ ,  $\varphi = \pi/3$  and  $N = 51$ , as time

evolves, we show the probability distribution ( $|\psi_j|^2$ ) of an excitation in Fig. 4 A and the total probability  $\sum_j |\psi_j|^2$  in Fig. 4 B. Even with the decay of excitation, we can still approximately extract the topological phase through  $\bar{P} \approx -0.5$ ; see the mean cell position of the light blue line in Fig. 4 C. For comparison, we also show the mean cell positions for the topological nontrivial phase with  $\theta = 2\pi/3$ ,  $\varphi = 2\pi/3$  (dark blue line) and trivial phases with  $\theta = \pi/3$ ,  $\varphi = 2\pi/3$  (red line) and  $\theta = 2\pi/3$ ,  $\varphi = \pi/3$  (yellow line).

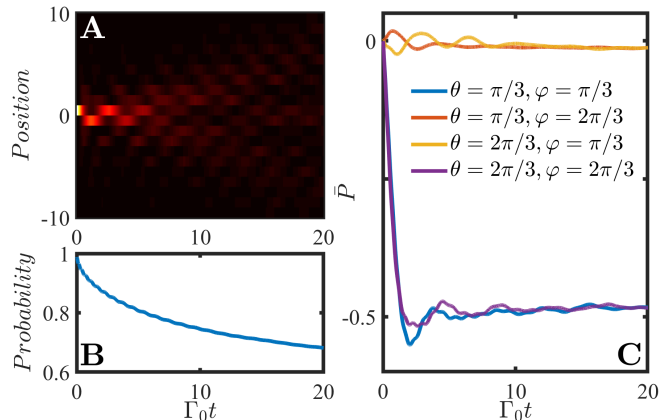


FIG. 3. **A** Quantum walks and **B** decay of excitation in topological nontrivial phase with  $(\theta = \pi/3, \varphi = \pi/3)$ . **C** Mean cell positions in different topological phases. The other parameters are chosen as  $\delta = 0.4$  and  $N = 51$ .

### Topology of photonic scattering

Because an excitation will generally decay into a photon in the long-time dynamics, it is highly appealing to explore how the topology of excitation is mapped to the topology of photonic scattering. We consider a photon with momentum ( $\kappa$ ) injected into the waveguide. After interacting with the emitters and transferring into excitation, or vice versa, the photon is either reflected or transmitted. The reflection and transmission coefficients are given by

$$r_\kappa = -i\Gamma_0 \sum_{j,j'} G_{j,j'}(\omega_\kappa) e^{i\omega_\kappa/c(z_j+z_{j'})}, \quad (7)$$

and

$$t_\kappa = 1 - i\Gamma_0 \sum_{j,j'} G_{j,j'}(\omega_\kappa) e^{i\omega_\kappa/c(z_{j'}-z_j)}, \quad (8)$$

which satisfy  $|r_\kappa|^2 + |t_\kappa|^2 = 1$  (see Supplementary Materials for more details). Here,  $G(\omega) = (\omega - H_{eff})^{-1}$  is the Green's function for an excitation. We calculate the reflection spectrum as a function of the inverse energy for the cases of trivial and topological nontrivial phases; see Figs. 4 A and D, respectively. When the photonic

	Topological nontrivial	Topological trivial
Even cell	1	0
Odd cell	0	1

TABLE I. Winding number for the trajectory of scattering textures (see Supplementary Materials for details).

frequency is in resonance with the subradiant states, the photon is completely transmitted, and there are  $N - 1$  ( $N$ ) dips for the topological nontrivial (trivial) phase in the shadow regions where the photonic frequency sweeps across the lower inverse band.

To show how the topological phase affects the scattering, we need to calculate the scattering textures  $s_i = \langle \psi_\kappa | \sigma_i | \psi_\kappa \rangle$  ( $i = x, y, z$ ), where  $\{|\psi_\kappa\rangle = (r_\kappa, t_\kappa)^T\}$  and  $\sigma_i$  are Pauli matrices. With the scattering textures  $\vec{s} = (s_x, s_y, s_z)$ , we can define the winding number of scattering along the  $x(y)$  direction as

$$\nu_{x(y)} = \int [\vec{s} \times \frac{\partial \vec{s}}{\partial \bar{\omega}}]_{x(y)} d\bar{\omega}. \quad (9)$$

where  $\bar{\omega}$  sweeps through the lower inverse band. Figs. 4 B and E show the trajectories of  $(s_y, s_z)$  as the inverse energy sweeps through the shadow regions for topological and trivial phases, respectively. We can visually estimate that the winding number along the  $x$  direction is close to 1 (0) in the topological nontrivial (trivial) phase. However,  $\nu_{x(y)}$  is generally not quantized along the  $x(y)$  directions. As the trajectories  $(s_x, s_y, s_z)$  in Figs. 4 C and F locate in a plane parallel to the  $z$  direction and depart from both the  $x$  and  $y$  directions, we can define a winding number around original point and along the direction perpendicular to the plane as

$$\nu = \sqrt{\nu_x^2 + \nu_y^2}. \quad (10)$$

We summarize the winding number in different topological phases with even and odd cells; see Table I. Remarkably, the winding number of the scattering textures depends on both the topological phase and the oddity of the cell numbers. We numerically find that a subradiant state contributes a  $\pi$  phase shift (see Supplementary Materials for details). Based upon the fact that there are  $(N - 1)$  subradiant states in a topological phase and  $N$  subradiant states in a trivial phase, we can reasonably argue that both the topological nontrivial phase with even cells and the trivial phase with odd cells contribute  $\pi$  phase to the scattering texture, leading to nontrivial quantization of winding number  $\nu$ .

### DISCUSSION

The topological inverse energy band actually reflects the topological phase of Green's function, which is directly related to the scattering of a photon. It means that the topological inverse band could be a powerful and

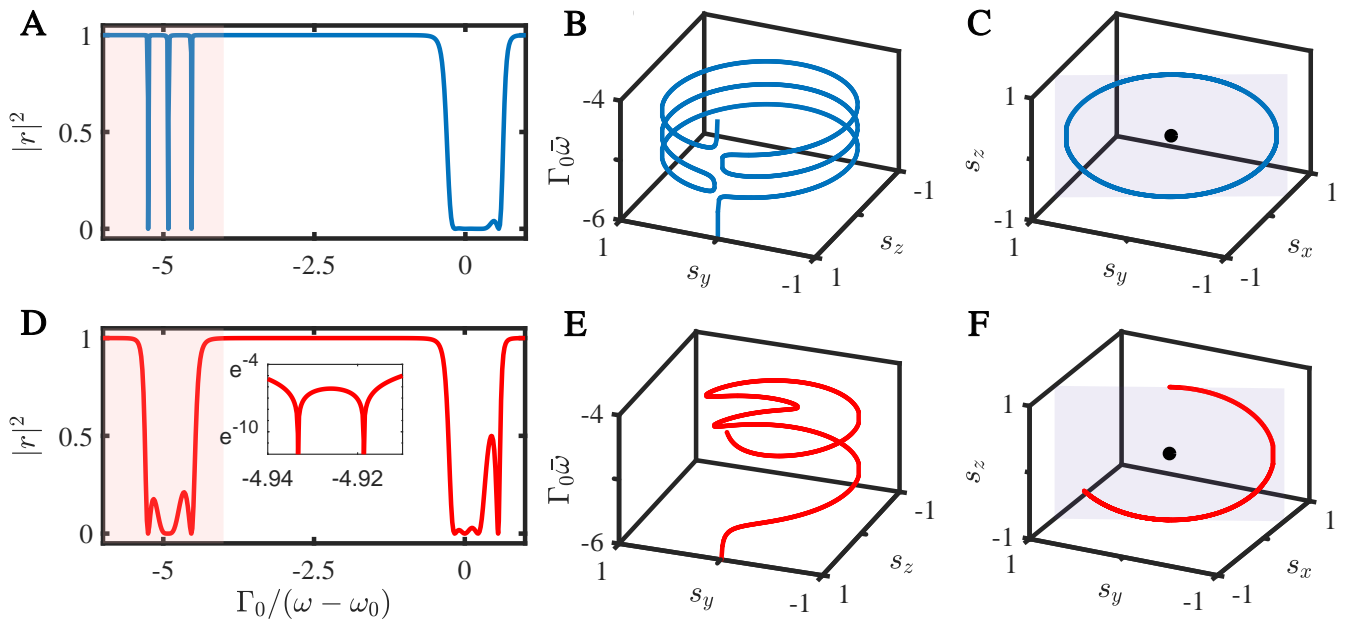


FIG. 4. Topology-dependent scattering in four cells. **A, D** Reflection as a function of inverse energy in topological and trivial phases, respectively. The inset of **d** enlarges its region with two nearby dips. **B, E** The scattering textures  $(s_y, s_z)$  as functions of the inverse energy in the shading regions for topological and trivial phases, respectively. **C, F** The trajectory of  $(s_x, s_y, s_z)$  as the inverse energy sweeps through the shading regions for topological and trivial phases, respectively. The parameters are chosen as  $N = 4$ ,  $g = 1$ ,  $\Gamma_0 = 0.01$ ,  $\omega_0 = 100$ ,  $\theta = 0$  and  $\theta = \pi$  for topological and trivial phases, respectively.

natural theoretical framework for predicting and tailoring novel topological-enriched light-matter interactions. We expect an unexplored richness in topological QED within the topological inverse band theory, considering higher dimensions that favor a variety of symmetries [24, 33], more photons that support quantum correlations and entanglement [17] and cavity mediated long-range interactions [34–36].

On the other hand, the group of dark Wannier states forms a decoherence-free subspace, in which Wannier dark states could be prepared, addressed, and accessed [37, 38]. Such structure could be a promising platform for quantum memory and quantum computation [39]. The collective radiation of the quantum emitters can significantly narrow the linewidth but maintain the resonant frequency. The narrower linewidth is beneficial for improving measurement precision of the resonant frequency. More importantly, the undisturbed resonant frequency plays the same role as a magic wavelength in optical lattice clocks [40]. Compared with individual atoms in optical lattice clocks, the collective radiation builds a coherent connection of all atoms and may be potentially used for next generation of precise frequency measurement.

## MATERIALS AND METHODS

**Bloch states and energy band.** To define the energy band, we consider an infinite and periodic array,

in which the eigenstates of excitation are Bloch states,

$$|\psi_{n,k}\rangle = \sum_{j,l} e^{ikqj} u_{n,k}(l) |qj + l\rangle. \quad (11)$$

Here,  $k \in [-\pi/q, +\pi/q]$  is quasimomentum,  $q = 2$  is the number of lattices in a unit cell,  $n$  is the band index,  $j$  is the cell index,  $l$  denotes the lattice index in a cell, and  $u_{n,k}$  are periodic functions of Bloch states. Substituting Eq. (11) into the Schrödinger equation  $H_{eff}|\psi_k\rangle = \omega_k|\psi_k\rangle$ , we obtain the equations for  $\{u_l\}$ ,

$$(\omega_k - \omega_0)/\Gamma_0 u_{n,k}(l') = \sum_{l=1}^2 H_k(l, l') u_{n,k}(l) \quad (12)$$

with the Bloch Hamiltonian matrix (see Supplementary Materials for details)

$$H_k(l, l') = \sin(\varphi|z_{l'} - z_l|) + \frac{i \sin(kq) \sin[\varphi(z_{l'} - z_l)]}{\cos(kq) - \cos(\varphi q)} + \frac{\sin(\varphi q) \cos[\varphi(z_{l'} - z_l)]}{\cos(kq) - \cos(\varphi q)}, \quad (13)$$

where the Hermitian matrix  $H_k = H_k^\dagger$ . This means that the energy band of the excitation becomes real because there is no way for the excitation to escape from an infinite array. From Eq. 13, we can deduce that the energy band is diverged at  $kq = \pm\varphi q + 2n\pi$ . However, the inverse energies  $\bar{\omega}_k = (\omega_k - \omega_0)^{-1}$  are always continuous function of momentum.

### Derivation of topological phase boundaries.

The Bloch Hamiltonian can be expressed as

$$H_k - \omega_0 I = \begin{pmatrix} a & b \\ b^* & a \end{pmatrix}. \quad (14)$$

with  $a = \frac{\sin(\varphi q)}{\cos(kq) - \cos(\varphi q)}$  and  $b = \sin(\varphi|\Delta z|) + \frac{\sin(\varphi q) \cos(\varphi|\Delta z|)}{\cos(kq) - \cos(\varphi q)} + \frac{i \sin(kq) \sin(\varphi|\Delta z|)}{\cos(kq) - \cos(\varphi q)}$ , where  $\Delta z = (z_2 - z_1)/d = 1 + 2\delta \cos \theta$ . The inverse of the Bloch Hamiltonian can be written as

$$\begin{aligned} (H_k - \omega_0 I)^{-1} &= \frac{1}{a^2 - |b|^2} \begin{pmatrix} a & -b \\ -b^* & a \end{pmatrix} \\ &= \frac{a}{a^2 - |b|^2} \begin{pmatrix} 1 & 0 \\ 0 & 1 \end{pmatrix} - \frac{1}{a^2 - |b|^2} \begin{pmatrix} 0 & b \\ b^* & 0 \end{pmatrix}. \end{aligned} \quad (15)$$

The topological phase transition happens when the eigenvalues of  $(H_k - \omega_0 I)^{-1}$  satisfy  $\bar{\omega}_{1,k} = \bar{\omega}_{2,k}$ . The transition point turns out to satisfy  $|b|^2 = 0$ . Moreover, the inverse energy band would be close at the momentum  $k = 0$  or  $k = \frac{\pi}{2}$ . In the case of  $k = 0$ ,  $|b|^2 = 0$  indicates that

$$\sin(\varphi|\Delta z|) = -\frac{\sin(\varphi q) \cos(\varphi|\Delta z|)}{1 - \cos(\varphi q)}. \quad (16)$$

We substitute the expression  $\Delta z = 1 + 2\delta \cos \theta$  and parameter  $q = 2$  into Eq. (16) and yield

$$\varphi = \pm \frac{(2n-1)\pi}{4\delta \cos \theta} \text{ or } \varphi = 2n\pi \quad (n = 1, 2, \dots). \quad (17)$$

Similarly, at  $k = \frac{\pi}{2}$ ,  $|b|^2 = 0$  indicates that

$$\sin(\varphi|\Delta z|) = \frac{\sin(\varphi q) \cos(\varphi|\Delta z|)}{1 + \cos(\varphi q)}. \quad (18)$$

In the similar circumstance with  $k = 0$ , at  $k = \frac{\pi}{2}$  we can

obtain the topological phase boundaries,

$$\varphi = \pm \frac{n\pi}{2\delta \cos \theta} \text{ or } \varphi = \pm \frac{(2n-1)\pi}{2} \text{ or } \theta = \frac{(2n-1)\pi}{2} \quad (19)$$

with positive integers  $n$ .

**Derivation of parameters for flat band.** When the inverse energy band is independent of  $k$ ,  $|b|^2$  should be a constant. The constant magnitude of the complex number  $b$  indicates that it should correspond to the value at  $k = 0$  as follows

$$\begin{aligned} &\sin^2(kq) \sin^2(\varphi|\Delta z|) + \\ &[\sin(\varphi q) \cos(\varphi|\Delta z|) + (\cos(kq) - \cos(\varphi q)) \sin(\varphi|\Delta z|)]^2 \\ &= \{\sin(\varphi q) \cos(\varphi|\Delta z|) + [1 - \cos(\varphi q)] \sin(\varphi|\Delta z|)\}^2. \end{aligned} \quad (20)$$

Simplifying Eq. (20), we obtain

$$4 \sin^2 \frac{kq}{2} \sin[(1 + 2\delta \cos \theta - q)\varphi] \sin[(1 + 2\delta \cos \theta)\varphi] = 0. \quad (21)$$

Utilizing the characteristics of trigonometric functions, we obtain the parametric equation about  $\theta$  and  $\varphi$ ,

$$(-1 + 2\delta \cos \theta)\varphi = \pm n\pi \text{ or } (1 + 2\delta \cos \theta)\varphi = \pm n\pi \quad (22)$$

with positive integers  $n$ .

## SUPPLEMENTARY MATERIALS

Supplementary material for this article is available at XXX. The Supplementary material is arranged as follow. Sec. S1. Derivation of effective Hamiltonian for the excitation; Sec. S2. Derivation of Bloch Hamiltonian in momentum space; Sec. S3. Dark states due to flat band; Sec. S4. Symmetric scale-free localization states due to radiative defects; Sec. S5. Green's function method; Sec. S6. Winding number of scattering textures; Sec. S7. Phase shift due to subradiant states. Refs. [17, 30, 41, 42] are included therein.

- 
- [1] P. Forn-Díaz, L. Lamata, E. Rico, J. Kono, and E. Solano, Ultrastrong coupling regimes of light-matter interaction, *Rev. Mod. Phys.* **91**, 025005 (2019).
- [2] R. Gutzler, M. Garg, C. R. Ast, K. Kuhnke, and K. Kern, Light-matter interaction at atomic scales, *Nature Reviews Physics* **3**, 441 (2021).
- [3] Atom-photon interactions: Basic process and applications, in *Atom-Photon Interactions: Basic Process and Applications* (John Wiley & Sons, Ltd, 1998) Chap. 2, pp. 67-163.
- [4] P. St-Jean, V. Goblot, E. Galopin, A. Lemaître, T. Ozawa, L. Le Gratiet, I. Sagnes, J. Bloch, and A. Amo, Lasing in topological edge states of a one-dimensional lattice, *Nature Photonics* **11**, 651 (2017).
- [5] M. A. Bandres, S. Wittek, G. Harari, M. Parto, J. Ren, M. Segev, D. N. Christodoulides, and M. Khajavikhan, Topological insulator laser: Experiments, *Science* **359**, eaar4005 (2018).
- [6] G. Harari, M. A. Bandres, Y. Lumer, M. C. Rechtsman, Y. D. Chong, M. Khajavikhan, D. N. Christodoulides, and M. Segev, Topological insulator laser: theory, *Science* **359**, eaar4003 (2018).
- [7] H.-R. Kim, M.-S. Hwang, D. Smirnova, K.-Y. Jeong, Y. Kivshar, and H.-G. Park, Multipolar lasing modes from topological corner states, *Nature communications* **11**, 1 (2020).
- [8] S. Kruk, A. Poddubny, D. Smirnova, L. Wang, A. Slobozhanyuk, A. Shorokhov, I. Kravchenko,

- B. Luther-Davies, and Y. Kivshar, Nonlinear light generation in topological nanostructures, *Nature nanotechnology* **14**, 126 (2019).
- [9] P. Lodahl, S. Mahmoodian, and S. Stobbe, Interfacing single photons and single quantum dots with photonic nanostructures, *Rev. Mod. Phys.* **87**, 347 (2015).
- [10] D. Roy, C. M. Wilson, and O. Firstenberg, Colloquium: Strongly interacting photons in one-dimensional continuum, *Rev. Mod. Phys.* **89**, 021001 (2017).
- [11] D. E. Chang, J. S. Douglas, A. González-Tudela, C.-L. Hung, and H. J. Kimble, Colloquium: Quantum matter built from nanoscopic lattices of atoms and photons, *Rev. Mod. Phys.* **90**, 031002 (2018).
- [12] A. S. Sheremet, M. I. Petrov, I. V. Iorsh, A. V. Poshakinskiy, and A. N. Poddubny, Waveguide quantum electrodynamics: collective radiance and photon-photon correlations, arXiv preprint arXiv:2103.06824 (2021).
- [13] S. Barik, A. Karasahin, C. Flower, T. Cai, H. Miyake, W. DeGottardi, M. Hafezi, and E. Waks, A topological quantum optics interface, *Science* **359**, 666 (2018).
- [14] M. Bello, G. Platero, J. I. Cirac, and A. González-Tudela, Unconventional quantum optics in topological waveguide qed, *Science advances* **5**, eaaw0297 (2019).
- [15] C. A. Downing, T. J. Sturges, G. Weick, M. Stobińska, and L. Martín-Moreno, Topological phases of polaritons in a cavity waveguide, *Phys. Rev. Lett.* **123**, 217401 (2019).
- [16] L. Wang, L. Yuan, X. Chen, and S. Fan, Single-photon transport in a topological waveguide from a dynamically modulated photonic system, *Phys. Rev. Applied* **14**, 014063 (2020).
- [17] Y. Ke, J. Zhong, A. V. Poshakinskiy, Y. S. Kivshar, A. N. Poddubny, and C. Lee, Radiative topological biphoton states in modulated qubit arrays, *Phys. Rev. Research* **2**, 033190 (2020).
- [18] H. Cai and D.-W. Wang, Topological phases of quantized light, *National Science Review* **8**, 10.1093/nsr/nwaa196 (2020), nwaa196, <https://academic.oup.com/nsr/article-pdf/8/1/nwaa196/38882031/nwaa196.pdf>.
- [19] J. Perczel, J. Borregaard, D. E. Chang, S. F. Yelin, and M. D. Lukin, Topological quantum optics using atomlike emitter arrays coupled to photonic crystals, *Phys. Rev. Lett.* **124**, 083603 (2020).
- [20] A. V. Poshakinskiy, J. Zhong, Y. Ke, N. A. Olekhno, C. Lee, Y. S. Kivshar, and A. N. Poddubny, Quantum hall phases emerging from atom-photon interactions, *npj Quantum Information* **7**, 1 (2021).
- [21] L. Leonforte, A. Carollo, and F. Ciccarello, Vacancy-like dressed states in topological waveguide qed, *Phys. Rev. Lett.* **126**, 063601 (2021).
- [22] W. Nie, T. Shi, F. Nori, and Y.-x. Liu, Topology-enhanced nonreciprocal scattering and photon absorption in a waveguide, *Phys. Rev. Applied* **15**, 044041 (2021).
- [23] E. Kim, X. Zhang, V. S. Ferreira, J. Banker, J. K. Iverson, A. Sipahigil, M. Bello, A. González-Tudela, M. Mirhosseini, and O. Painter, Quantum electrodynamics in a topological waveguide, *Phys. Rev. X* **11**, 011015 (2021).
- [24] D. De Bernardis, Z.-P. Ciani, I. Carusotto, M. Hafezi, and P. Rabl, Light-matter interactions in synthetic magnetic fields: Landau-photon polaritons, *Phys. Rev. Lett.* **126**, 103603 (2021).
- [25] J.-S. Tang, W. Nie, L. Tang, M. Chen, X. Su, Y. Lu, F. Nori, and K. Xia, Nonreciprocal single-photon band structure, *Phys. Rev. Lett.* **128**, 203602 (2022).
- [26] P. Jiang, N. Ma, X. Qiao, and H. Zhang, Recent progress in chiral topological quantum interface, *Frontiers in Physics* , 22 (2022).
- [27] A. Bansil, H. Lin, and T. Das, Colloquium: Topological band theory, *Rev. Mod. Phys.* **88**, 021004 (2016).
- [28] T. Ozawa, H. M. Price, A. Amo, N. Goldman, M. Hafezi, L. Lu, M. C. Rechtsman, D. Schuster, J. Simon, O. Zeitlinger, and I. Carusotto, Topological photonics, *Rev. Mod. Phys.* **91**, 015006 (2019).
- [29] Y. Marques, I. A. Shelykh, and I. V. Iorsh, Bound photonic pairs in 2d waveguide quantum electrodynamics, *Phys. Rev. Lett.* **127**, 273602 (2021).
- [30] Y. Ke, A. V. Poshakinskiy, C. Lee, Y. S. Kivshar, and A. N. Poddubny, Inelastic scattering of photon pairs in qubit arrays with subradiant states, *Phys. Rev. Lett.* **123**, 253601 (2019).
- [31] S. Longhi, Probing one-dimensional topological phases in waveguide lattices with broken chiral symmetry, *Opt. Lett.* **43**, 4639 (2018).
- [32] Z.-Q. Jiao, S. Longhi, X.-W. Wang, J. Gao, W.-H. Zhou, Y. Wang, Y.-X. Fu, L. Wang, R.-J. Ren, L.-F. Qiao, and X.-M. Jin, Experimentally detecting quantized zak phases without chiral symmetry in photonic lattices, *Phys. Rev. Lett.* **127**, 147401 (2021).
- [33] C. Vega, D. Porrás, and A. González-Tudela, Topological multi-mode waveguide QED, arXiv preprint arXiv:2207.02090 (2022).
- [34] V. D. Vaidya, Y. Guo, R. M. Kroeze, K. E. Ballantine, A. J. Kollár, J. Keeling, and B. L. Lev, Tunable-range, photon-mediated atomic interactions in multimode cavity qed, *Phys. Rev. X* **8**, 011002 (2018).
- [35] T. Chanda, R. Kraus, G. Morigi, and J. Zakrzewski, Self-organized topological insulator due to cavity-mediated correlated tunneling, *Quantum* **5**, 501 (2021).
- [36] F. Mivehvar, F. Piazza, T. Donner, and H. Ritsch, Cavity qed with quantum gases: new paradigms in many-body physics, *Advances in Physics* **70**, 1 (2021).
- [37] M. Zanner, T. Orell, C. M. Schneider, R. Albert, S. Oleschko, M. L. Juan, M. Silveri, and G. Kirchmair, Coherent control of a multi-qubit dark state in waveguide quantum electrodynamics, *Nature Physics* **18**, 538 (2022).
- [38] R. Holzinger, R. Gutierrez-Jauregui, T. Hönl-Deerinis, G. Kirchmair, A. Asenjo-Garcia, and H. Ritsch, Control of Localized Single- and Many-Body Dark States in Waveguide QED, *Phys. Rev. Lett.* **129**, 253601 (2022).
- [39] V. Paulisch, H. J. Kimble, and A. González-Tudela, Universal quantum computation in waveguide QED using decoherence free subspaces, *New Journal of Physics* **18**, 043041 (2016).
- [40] S. L. Campbell, R. Hutson, G. Marti, A. Goban, N. Darkwah Oppong, R. McNally, L. Sonderhouse, J. Robinson, W. Zhang, B. Bloom, *et al.*, A fermi-degenerate three-dimensional optical lattice clock, *Science* **358**, 90 (2017).
- [41] J.-T. Shen and S. Fan, Strongly correlated two-photon transport in a one-dimensional waveguide coupled to a two-level system, *Phys. Rev. Lett.* **98**, 153003 (2007).
- [42] L. Li, C. H. Lee, and J. Gong, Impurity induced scale-free localization, *Communications Physics* **4**, 1 (2021).

## ACKNOWLEDGMENTS

We acknowledge useful discussions with A. N. Poddubny, L. Lin, and L. Zhang. **Funding and support:** This work is supported by the National Key Research and Development Program of China (Grant No. 2022YFA1404104), the National Natural Science Foundation of China (Grant No. 12025509 and 12275365), and the Key-Area Research and Development Program of Guangdong Province (Grant No. 2019B030330001). Y. Kivshar is supported by the Australian Research Coun-

cil (Grant No. DP210101292). **Author contributions:** Y. Ke and C. Lee conceived the idea. Y. Ke, J. Huang and W. Liu carried out analytical and numerical calculations. C. Lee and Y. Kivshar supervised the project. Y. Ke wrote the first version of the manuscript. All authors contributed extensively to the interpretation of the results and the writing of the paper. **Competing interests:** The authors declare no competing interests. **Data and materials availability:** All data needed to evaluate the conclusions in the paper are present in the paper and/or the Supplementary Materials.

## Supplemental Materials:

### Topological inverse band theory in waveguide quantum electrodynamics

Yongguan Ke<sup>1,2,3</sup>, Jiakuan Huang<sup>2</sup>, Wenjie Liu<sup>2,3</sup>, Yuri Kivshar<sup>4,\*</sup>, Chaohong Lee<sup>1,2,3,†</sup>

<sup>1</sup> College of Physics and Optoelectronic Engineering, Shenzhen University, Shenzhen 518060, China

<sup>2</sup> Guangdong Provincial Key Laboratory of Quantum Metrology and Sensing & School of Physics and Astronomy, Sun Yat-Sen University (Zhuhai Campus), Zhuhai 519082, China

<sup>3</sup> State Key Laboratory of Optoelectronic Materials and Technologies, Sun Yat-Sen University (Guangzhou Campus), Guangzhou 510275, China

<sup>4</sup> Nonlinear Physics Center, Research School of Physics, Australian National University, Canberra, Australian Capital Territory, Australia.

#### S1. DERIVATION OF EFFECTIVE HAMILTONIAN FOR THE EXCITATION

We consider the propagation of photons in a waveguide coupled to two-level atoms with quasiperiodic spacing, which is characterized by the Hamiltonian in real space that contains three parts [1],

$$H_R = H_A + H_F + H_I. \quad (S1)$$

Here,  $H_A$  describes the energy of excitations,

$$H_A = \sum_j \hbar\omega_0 b_j^\dagger b_j \quad (S2)$$

where  $\omega_0$  is the uniform resonant frequency of the two levels in atoms,  $b_j^\dagger$  ( $b_j$ ) is the excitation creation (annihilation) operator on the  $j$ th atom.  $H_F$  describes the propagating photon in the waveguide along the  $z$  direction with light velocity  $c$ ,

$$H_F = i\hbar c \int_{-\infty}^{+\infty} dz [a_L^\dagger(z) \frac{\partial}{\partial z} a_L(z) - a_R^\dagger(z) \frac{\partial}{\partial z} a_R(z)], \quad (S3)$$

where  $a_L^\dagger(z)$  ( $a_L(z)$ ) and  $a_R^\dagger(z)$  ( $a_R(z)$ ) are the creation (annihilation) operators for a photon propagating to the left and right at position  $z$ , respectively.  $H_I$  describes the interaction between excitation and photon,

$$H_I = \sum_{j=1}^N \hbar g \int dz \delta(z - z_j) [(a_L^\dagger(z) + a_R^\dagger(z)) b_j + h.c.], \quad (S4)$$

where  $g$  is the coupling strength, and the total number of atoms is  $N$ . The position of the  $j$ th atom is given by

$$z_j = d[j + \delta \cos(2\pi\beta j + \theta)], \quad (S5)$$

where  $d$  is the spacing constant,  $\delta$  is the quasi-periodic strength,  $\beta$  is the modulation frequency and  $\theta$  is the modulation phase. The qubit positions become quasiperiodic when  $\beta$  is an irrational number.

Alternatively, by making a Fourier transform,

$$\begin{aligned} a_L(z) &= \frac{1}{\sqrt{2\pi}} \int_{-\infty}^0 a(k) e^{ikz} dk, \\ a_R(z) &= \frac{1}{\sqrt{2\pi}} \int_0^{+\infty} a(k) e^{ikz} dk, \end{aligned} \quad (S6)$$

we can derive the Hamiltonian in the momentum space,

$$\begin{aligned} H_M &= \int_{-\infty}^{+\infty} \hbar\omega_k a(k)^\dagger a(k) dk + \sum_j \hbar\omega_0 b_j^\dagger b_j \\ &+ \frac{\hbar g}{\sqrt{2\pi}} \sum_j \int_{-\infty}^{+\infty} (b_j^\dagger a(k) e^{ikz_j} + b_j a(k)^\dagger e^{-ikz_j}) dk. \end{aligned} \quad (S7)$$

Here,  $a(k)$  is the annihilation operator for a photon with a wave vector  $k$ .  $\omega_k = c|k|$  is the frequency of a single photon with light velocity  $c$ .

We write an ansatz for a general state in the waveguide QED as

$$|\psi\rangle = \int dk f_k a_k^\dagger |0\rangle + \sum_j \psi_j b_j^\dagger |0\rangle. \quad (\text{S8})$$

Here,  $\psi_j$  is the amplitude of the  $j$ -th atom being excited,  $f_k$  is the amplitude of the photon in the mode  $k$ , and  $|0\rangle$  is the vacuum state with all atoms in the ground states and no photons. Substituting this ansatz (S8) and the Hamiltonian (S7) into the Schrödinger equation,  $H_{eff}|\psi\rangle = \hbar\omega|\psi\rangle$ , we can obtain the following equation,

$$\int dk (\omega_k f_k + \sum_j \frac{g}{\sqrt{2\pi}} e^{-ikz_j} \psi_j - \omega f_k) a_k^\dagger |0\rangle + \sum_j (\omega_0 \psi_j + \int dk \frac{g}{\sqrt{2\pi}} e^{ikz_j} f_k - \omega \psi_j) b_j^\dagger |0\rangle = 0. \quad (\text{S9})$$

Consequently, we get the coupling relations between  $\psi_j$  and  $f_k$ ,

$$\begin{aligned} \sum_j \frac{g}{\sqrt{2\pi}} e^{-ikz_j} \psi_j &= (\omega - \omega_k) f_k \\ \int dk \frac{g}{\sqrt{2\pi}} e^{ikz_j} f_k &= (\omega - \omega_0) \psi_j \end{aligned} \quad (\text{S10})$$

Eliminating  $f_k$ , we can obtain an effective eigen-equation for excitation,

$$\omega_0 \psi_j + g^2 \sum_{j'} \int \frac{dk}{2\pi} \frac{e^{ik(z_j - z_{j'})}}{\omega - \omega_k} \psi_{j'} = \omega \psi_j. \quad (\text{S11})$$

Using the Cauchy's integral formula, we can simplify the above equation as

$$\omega_0 \psi_j - i\Gamma_0 \sum_{j'} e^{i\omega/c|z_j - z_{j'}|} \psi_{j'} = \omega \psi_j \quad (\text{S12})$$

where  $\Gamma_0 = \frac{g^2}{c}$  is the radiative decay rate. Hence, the motion of an excitation in the qubit array is governed by

$$H_{eff} = \sum_j \omega_0 b_j^\dagger b_j - i\Gamma_0 \sum_{j,j'} e^{i\omega/c|z_j - z_{j'}|} b_j^\dagger b_{j'} \quad (\text{S13})$$

## S2. DERIVATION OF BLOCH HAMILTONIAN IN MOMENTUM SPACE

The position of the  $j$ th qubit is given by

$$z_j = d [j + \delta \cos(2\pi\beta j + \theta)]. \quad (\text{S14})$$

For arbitrary  $m, n$ , we obtain the difference between  $z_m$  and  $z_n$ ,

$$\frac{z_m - z_n}{d} = m - n - 2\delta \sin(2\pi\beta \frac{m+n}{2} + \theta) \sin(2\pi\beta \frac{m-n}{2}) \quad (\text{S15})$$

We use the cell index  $j$  and the sublattice index  $l$  to mark  $m, n$ , that is,  $m = qj' + l'$  and  $n = qj + l$ . where  $q = 2$  is the length of the primitive cell. With these notations, we can reshape Eq. (S15) to

$$\frac{z_m - z_n}{d} = (qj' + l') - (qj + l) - 2\delta \sin(2\pi\beta \frac{l+l'}{2} + \theta) \sin(2\pi\beta \frac{l'-l}{2}). \quad (\text{S16})$$

The eigenstates of the effective Hamiltonian in real space satisfy

$$\omega_k |\psi_k\rangle = H_{eff} |\psi_k\rangle, \quad (\text{S17})$$

with the Bloch states

$$|\psi_k\rangle = \sum_{j,l} e^{ikqj} u_l |qj + l\rangle, \quad (\text{S18})$$

and the eigenvalues  $\omega_k$ . We multiply Eq. (S17) by  $\langle qj' + l' |$  and obtain  $u_{l'}$  satisfying

$$(\omega_k - \omega_0)u_{l'} = -i\Gamma_0 \sum_{j,l} e^{i\varphi|(qj'+l')-(qj+l)-2\delta \sin(2\pi\beta\frac{l'+l}{2}+\theta) \sin(2\pi\beta\frac{l'-l}{2})} |u_l e^{ikq(j-j')} \quad (\text{S19})$$

Removing the absolute value, we get the expression,

$$\begin{aligned} (\omega_k - \omega_0)u_{l'} &= -i\Gamma_0 \sum_{j'>j}^N e^{i\varphi[l'-l-2\delta \sin(2\pi\beta\frac{l'+l}{2}+\theta) \sin(2\pi\beta\frac{l'-l}{2})]} e^{i(k-\varphi)q(j-j')} u_l \\ &\quad - i\Gamma_0 \sum_{j'<j}^N e^{i\varphi[l'-l-2\delta \sin(2\pi\beta\frac{l'+l}{2}+\theta) \sin(2\pi\beta\frac{l'-l}{2})]} e^{i(k+\varphi)q(j-j')} u_l \\ &\quad - i\Gamma_0 \sum_{l' \neq l}^N e^{i\varphi[l'-l-2\delta \sin(2\pi\beta\frac{l'+l}{2}+\theta) \sin(2\pi\beta\frac{l'-l}{2})]} u_l \\ &\quad - i\Gamma_0 \delta(l-l') u_l \end{aligned} \quad (\text{S20})$$

After a series of simplification, we can obtain the equation below,

$$\begin{aligned} (\omega_k - \omega_0)u_{l'} &= i\Gamma_0 \frac{\sin(kq)}{\cos(kq) - \cos(\varphi q)} \sum_l \sin \left\{ \varphi[l' - l - 2\delta \sin(2\pi\beta\frac{l'+l}{2} + \theta) \sin(2\pi\beta\frac{l'-l}{2})] \right\} u_l \\ &\quad + \Gamma_0 \frac{\sin(\varphi q)}{\cos(kq) - \cos(\varphi q)} \sum_l \cos \left\{ \varphi[l' - l - 2\delta \sin(2\pi\beta\frac{l'+l}{2} + \theta) \sin(2\pi\beta\frac{l'-l}{2})] \right\} u_l \\ &\quad + \Gamma_0 \sum_{l'>l} \sin \left\{ \varphi[l' - l - 2\delta \sin(2\pi\beta\frac{l'+l}{2} + \theta) \sin(2\pi\beta\frac{l'-l}{2})] \right\} u_l \\ &\quad - \Gamma_0 \sum_{l'<l} \sin \left\{ \varphi[l' - l - 2\delta \sin(2\pi\beta\frac{l'+l}{2} + \theta) \sin(2\pi\beta\frac{l'-l}{2})] \right\} u_l \end{aligned} \quad (\text{S21})$$

Finally, we have  $(\omega_k - \omega_0)/\Gamma_0 u_{l'} = \sum_{l=1} H_k(l, l') u_l$  with the elements of the Bloch Hamiltonian in the momentum space,

$$H_k(l, l') = \sin\left(\varphi \frac{|z_{l'} - z_l|}{d}\right) + \frac{\sin(\varphi q) \cos\left(\varphi \frac{|z_{l'} - z_l|}{d}\right)}{\cos(kq) - \cos(\varphi q)} + \frac{i \sin(kq) \sin\left(\varphi \frac{|z_{l'} - z_l|}{d}\right)}{\cos(kq) - \cos(\varphi q)}, \quad (\text{S22})$$

where  $\varphi = \omega_0 d/c$  is the phase constant.

### S3. DARK STATES DUE TO FLAT BAND

For the flat band, the group velocity is zero and the effective mass tends to infinite. It means that an excitation will stay in the atomic arrays with zero decay rate. Here, we show the decay rate of the most subradiant state as a function of  $\theta$  and  $\varphi$ ; see Fig. S1. We can find the minimal decay rate in the parameters that support flat band. The data reaches its limit of machine precision around  $10^{-14}$ , which can be viewed as zero decay rate.

### S4. SYMMETRIC SCALE-FREE LOCALIZATION STATES DUE TO RADIATIVE DEFECTS

Below we discuss how radiative defects affect the bulk-edge correspondence. We show the density distribution and the inverse participation ratio (IPR) of each eigenstate for topological nontrivial phase ( $\varphi = 1, \theta = 0$ ) and trivial ( $\varphi = 1, \theta = \pi$ ) phase in Fig. S2. Unlike the edge states in the gap between continuous inverse bands for topological nontrivial phase, the results in Fig. S2 indicate that localization states exist in the upper band for the topological nontrivial phase while in both upper and lower inverse bands for the trivial one. Numerically, we find that  $(H_{eff} - \omega_0)^{-1}$  corresponds to a SSH model with radiative defects at two endpoints in the following form:

$$\frac{1}{H_{eff} - \omega_0} = \sum_{j=1}^{N-1} \left( v c_{A,j}^\dagger c_{B,j} + w c_{B,j}^\dagger c_{A,j+1} + \text{h.c.} \right) + D(n_{A,1} + n_{B,N}) + C. \quad (\text{S23})$$

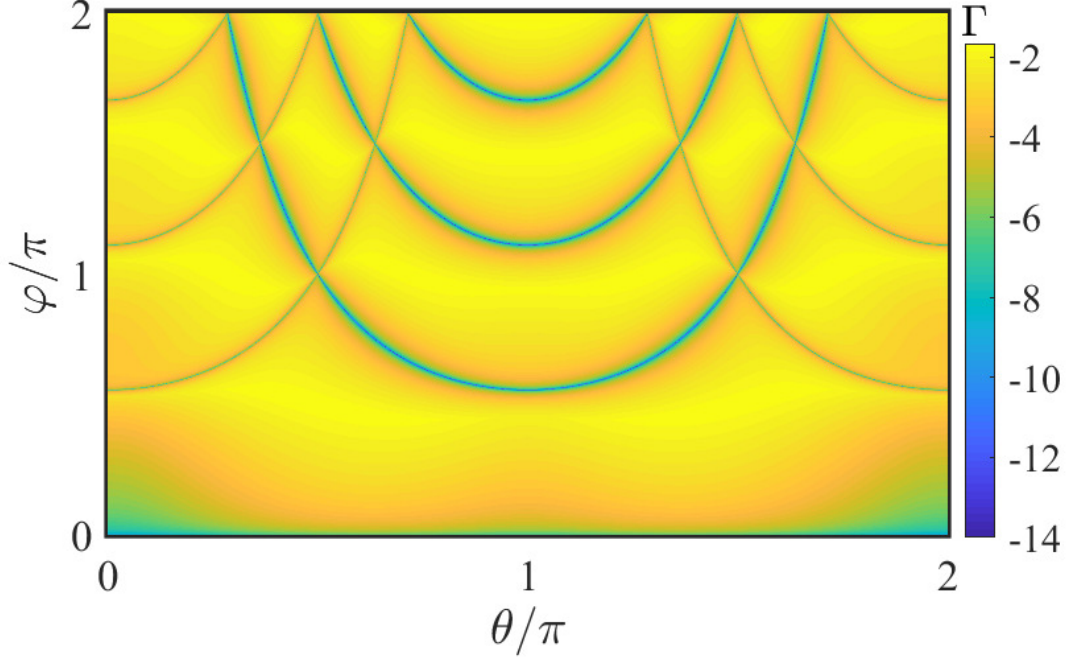


FIG. S1. The decay rate of the most subradiant state as a function of modulation phase and phase constant. The other parameters are chosen as  $\Gamma_0 = 1$ ,  $\delta = 0.4$ , and  $N = 4$ .

$v$  and  $w$  respectively denote the intra-cell and inter-cell hopping strengths, the radiative defect  $D$  is a complex number, and  $C$  is an energy constant. Considering a semi-infinite model with a neglected energy constant  $C$ , the amplitudes between different sites are obtained in terms of the eigenequation  $(H - E)|\Psi\rangle = 0$ :

$$\begin{aligned}
 w\psi_{0,B} + (D - E)\psi_{1,A} + v\psi_{1,B} &= 0 \\
 v\psi_{1,A} - E\psi_{1,B} + w\psi_{2,A} &= 0 \\
 w\psi_{1,B} - E\psi_{2,A} + v\psi_{2,B} &= 0 \\
 &\vdots \\
 v\psi_{N-1,A} - E\psi_{N-1,B} + w\psi_{N,A} &= 0 \\
 w\psi_{N-1,B} - E\psi_{N,A} + v\psi_{N,B} &= 0.
 \end{aligned} \tag{S24}$$

From the recurrence relation (S24), it yields

$$\begin{pmatrix} \psi_{N,B} \\ \psi_{N,A} \end{pmatrix} = M^{N-1} M_0 \begin{pmatrix} \psi_{1,A} \\ \psi_{0,B} \end{pmatrix} \tag{S25}$$

with

$$M_0 = \begin{pmatrix} \frac{-D+E}{v} & -\frac{w}{v} \\ 1 & 0 \end{pmatrix}, M = \begin{pmatrix} \frac{E^2}{vw} - \frac{w}{v} & -\frac{E}{w} \\ \frac{E}{w} & -\frac{v}{w} \end{pmatrix}. \tag{S26}$$

The initial conditions are set as  $N \rightarrow \infty$ ,  $\psi_{0,B} = 0$ ,  $\psi_{1,A} = 1$ . In the thermodynamic limit  $N \rightarrow \infty$ , the bulk-energies keep the same as those in the conventional SSH model,

$$H_k = (v + w \cos k)\sigma_x + w \sin k \sigma_y \tag{S27}$$

with the energy

$$E_k = \pm \sqrt{v^2 + w^2 + 2vw \cos k}. \tag{S28}$$

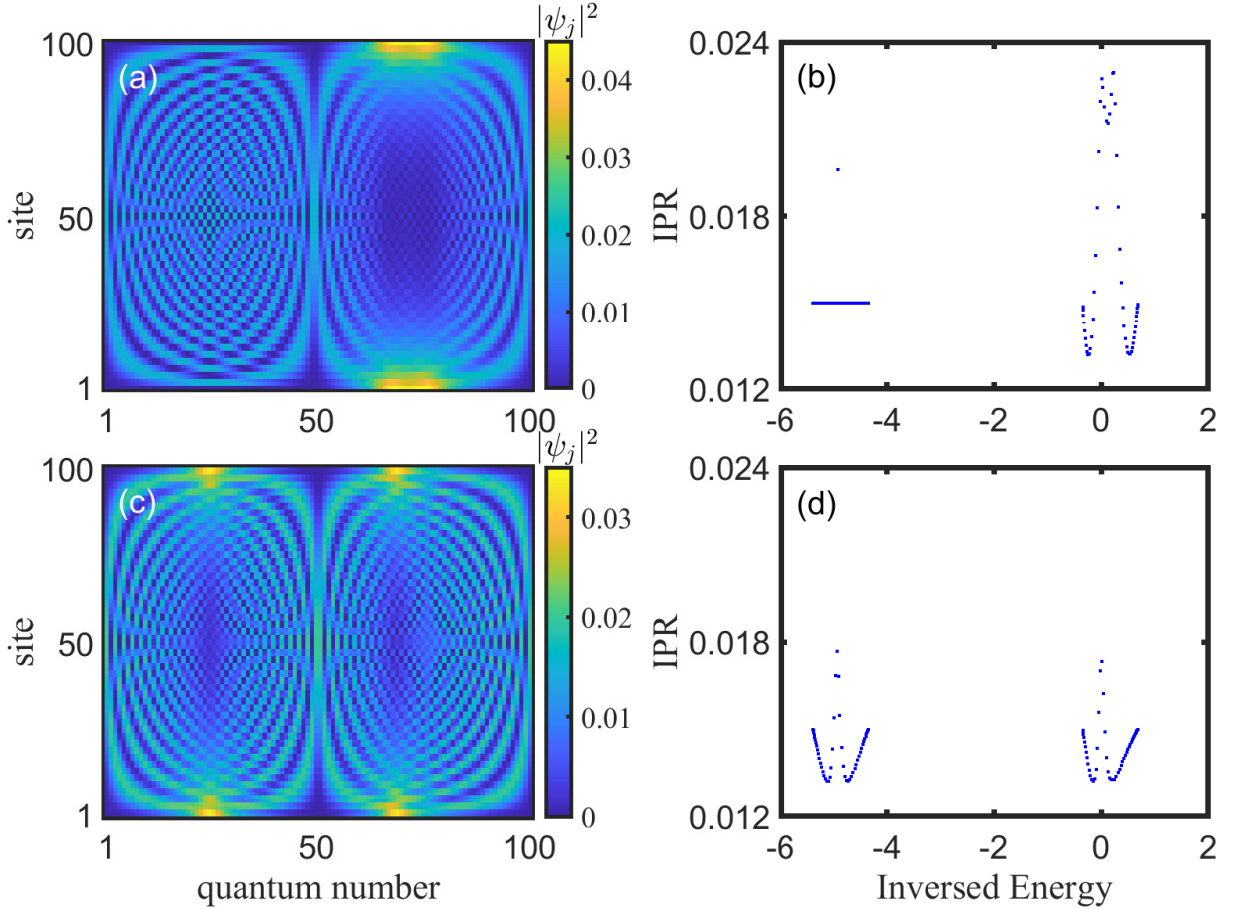


FIG. S2. (a) and (c): density distribution of each eigenstate respectively with  $\theta = 0$  and  $\theta = \pi$ . The quantum number is ordered for increasing values of the inversed energy. (b) and (d) respectively correspond to the IPR of eigenstate in (a) and (c). The other parameters are chosen as  $\varphi = 1$ ,  $\Gamma_0 = 1$  and  $\delta = 0.4$ .

Therefore, the bulk energies satisfy  $(w - v)^2 \leq E^2 \leq (w + v)^2$ . We first deal with

$$\begin{pmatrix} \frac{-D+E}{v} & -\frac{w}{v} \\ 1 & 0 \end{pmatrix} \begin{pmatrix} \psi_{1,A} \\ \psi_{0,B} \end{pmatrix} = \begin{pmatrix} \frac{-D+E}{v} \\ 1 \end{pmatrix} = \Phi. \quad (\text{S29})$$

By solving  $Mu_{\pm} = \varepsilon_{\pm}u_{\pm}$ , we obtain the corresponding eigenvalues  $\varepsilon_{\pm}$  and eigenstates  $u_{\pm}$  with  $\varepsilon_{\pm} = (\alpha \pm \sqrt{\alpha^2 - 4})/2$  and  $\varepsilon_+\varepsilon_- = 1$ . Here  $\alpha = \frac{E^2 - w^2 - v^2}{wv}$ . The state  $\Phi$  can be expanded as  $\Phi = au_+ + bu_-$ , then Eq. (S25) turns out to be

$$\begin{pmatrix} \psi_{N,B} \\ \psi_{N,A} \end{pmatrix} = a\varepsilon_+^{N-1}u_+ + b\varepsilon_-^{N-1}u_-. \quad (\text{S30})$$

There exists  $|\varepsilon_+| < 1$  or  $|\varepsilon_-| < 1$  when  $E^2 > (w + v)^2$  or  $E^2 < (w - v)^2$ , which means that the appearance of the edge state is accompanied by its energy isolated from continuous bands. Until now, we have demonstrated that localization states in the continuous spectrum in Fig. S2 not belong to edge states with  $|\psi_j|^2 \sim e^{-\alpha j}$ .

To explore the properties of localization states, we show the density distribution of the maximum IPR for a fixed system size ( $N = 50$ ) in Fig. S3(a) and the change of the maximum IPR as the system size increases in Fig. S3(b). The other parameters are chosen as  $\beta = 1/2$ ,  $\varphi = 1$ ,  $\Gamma_0 = 1$ ,  $\delta = 0.4$  and  $\theta = 0$ . The fitted result in Fig. S3(a) with red dotted line reflects that the localization state satisfies  $|\psi_j|^2 \sim (e^{-\alpha j/N} + e^{\alpha j/N})^2$  with  $\alpha \approx -4.848$ , whose IPR exhibited in Fig. S3(b) with red circles agrees with the maximum IPR of  $(H_{eff} - \omega_0)^{-1}$  with blue dots. Once the radiative defect is absent, Eq. (S23) is restored to the celebrated SSH model. To make a comparison, we artificially set  $D = 0$  to add the IPR of edge states in Fig. S3(b) with green crosses. Different from the edge states, the IPR of the localized state sensitively depends on the system size. It allows us to class localization states as scale-free localization with weak boundary accumulation [2]. Unlike the weak boundary accumulation toward one direction,

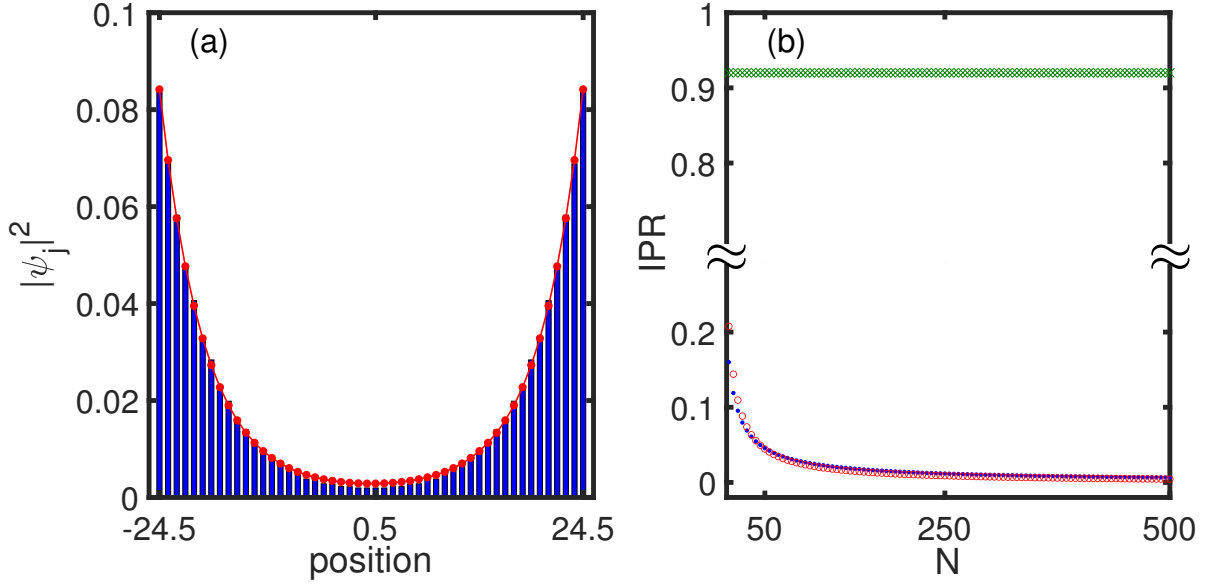


FIG. S3. (a) The density distribution of eigenstate with the maximum IPR for  $N = 50$ . The red dotted line is the fitted result  $|\psi_j|^2 \sim (e^{-\alpha j/N} + e^{\alpha j/N})^2$  with  $\alpha \approx -4.848$ . (b) The maximum IPR as a function of system size for topological nontrivial phase with  $\theta = 0$ . The blue dots denote the result of  $(H_{eff} - \omega_0)^{-1}$  and the green crosses are its corresponding edge states in Eq. (S23) but  $D = 0$ . The IPR of fitted localized state is marked by red circles. The other parameters are chosen as  $\varphi = 1$ ,  $\Gamma_0 = 1$  and  $\delta = 0.4$ .

there are symmetric scale-free localization states due to symmetric radiative defects at two endpoints. Therefore, the bulk-edge correspondence is destroyed because radiative defects give rise to partially symmetric scale-free localization states in the continuous spectrum.

### S5. GREEN'S FUNCTION METHOD

We can alternatively use the Green's function method to calculate the reflection and transmission. First, we separate the Hamiltonian (S7) in momentum space into two parts,  $H_M = H_0 + V$ , with

$$H_0 = \int_{-\infty}^{+\infty} \hbar\omega_k a(k)^\dagger a(k) dk + \sum_j \hbar\omega_0 b_j^\dagger b_j \quad (\text{S31})$$

and

$$V = \frac{\hbar g}{\sqrt{2\pi}} \sum_j \int_{-\infty}^{+\infty} (b_j^\dagger a(k) e^{ikz_j} + b_j a(k)^\dagger e^{-ikz_j}) dk. \quad (\text{S32})$$

The scattering problem can be solved by the famous Lippmann-Schwinger equation,

$$|\psi_{out}\rangle = |\psi_{in}\rangle + \frac{1}{E - H_0} V |\psi_{out}\rangle, \quad (\text{S33})$$

where  $|\psi_{in}\rangle = a(\kappa)^\dagger |0\rangle$  indicates that a input photon with a wave vector  $\kappa > 0$  and frequency  $\omega = c|\kappa|$  is propagating rightward. The output states are given by

$$|\psi_{out}\rangle = \sum_j Q_j b_j^\dagger |0\rangle + \int P_k a(k)^\dagger |0\rangle dk. \quad (\text{S34})$$

Substituting the input and output states into Eq. (S33), we can obtain the relation between  $P_k$  and  $Q_j$ ,

$$P_k = \delta(k, \kappa) + \frac{g}{\sqrt{2\pi}} \sum_j \frac{e^{-ikz_j}}{\omega - c|k|} Q_j; \quad (\text{S35})$$

$$Q_j = \frac{g}{\sqrt{2\pi}} \int \frac{e^{ikz_j}}{\omega - \omega_0} P_k dk. \quad (\text{S36})$$

Combining the above equations, we can obtain the relations for the motion of an excitation,

$$Q_j = \frac{g}{\sqrt{2\pi}} \frac{e^{i\kappa z_j}}{\omega - \omega_0} - i\Gamma_0 \sum_{j'} \frac{e^{i\omega/c|z_j - z_{j'}|}}{\omega - \omega_0} Q_{j'}, \quad (\text{S37})$$

where we have used a formula

$$\frac{g^2}{2\pi} \int \frac{e^{ik(z_j - z_{j'})}}{\omega - c|k|} dk = -i \frac{g^2}{c} e^{i\omega/c|z_j - z_{j'}|}. \quad (\text{S38})$$

The propagation of an excitation in the qubit array is governed by the Green's function, which is determined by

$$G^{-1}(\omega) = \omega - H_{eff}, \quad (\text{S39})$$

with the effective Hamiltonian for excitation [3, 4],

$$H_{eff} = \sum_j \omega_0 b_j^\dagger b_j - i\Gamma_0 \sum_{j,l} b_j^\dagger b_l e^{i\omega/c|z_l - z_j|}. \quad (\text{S40})$$

Here,  $\Gamma_0 = g^2/c$  is the radiative decay rate, and the phase constant is defined as  $\varphi = \omega d/c$ , depending on the frequency of an input photon  $\omega$ , spacing constant  $d$  and the light velocity  $c$ . The hopping of excitation from  $z_l$  to  $z_j$  points is assisted by the photon emitted from the  $l$ th qubit and consequently reabsorbed by the  $j$ th qubit. When the spacing constant is small enough, the phase constant in the effective Hamiltonian can be replaced by  $\varphi = \omega_0 d/c$ , which is the so-called Markov approximation [30].

Combining Eqs. (S37) and (S39), the excitation amplitudes  $Q_j$  are given by

$$Q_j = \frac{g}{\sqrt{2\pi}} \sum_{j'} G_{j,j'}(\omega) e^{i\kappa z_{j'}}. \quad (\text{S41})$$

Substituting Eq. (S41) into Eq. (S35), we can obtain the output field distribution

$$P_k = \delta(k, \kappa) + \frac{g^2}{2\pi} \sum_{j,j'} G_{j,j'}(\omega_\kappa) \frac{e^{-ikz_j + i\kappa z_{j'}}}{\omega - c|k|}. \quad (\text{S42})$$

The reflection coefficient is given by

$$r_\kappa = \int_{-\infty}^0 P_k dk = -i\Gamma_0 \sum_{j,j'} G_{j,j'}(\omega_\kappa) e^{i\omega_\kappa/c(z_j + z_{j'})}, \quad (\text{S43})$$

and the transmission is given by

$$t_\kappa = \int_0^{+\infty} P_k dk = 1 - i\Gamma_0 \sum_{j,j'} G_{j,j'}(\omega_\kappa) e^{i\omega_\kappa/c(z_{j'} - z_j)}, \quad (\text{S44})$$

and they also satisfy  $|r_\kappa|^2 + |t_\kappa|^2 = 1$ .

Because the reflection can be immediately obtained once the transmission is known, we focus on the reflection of a single photon. To make it clear, we expand the Green function in terms of the eigenvalues  $\{\omega_n\}$  and the eigenstates  $\{\psi_n\}$  of the effective Hamiltonian,

$$G_{j,j'}(\omega_\kappa) = \sum_n \frac{\psi_n(j)\psi_n(j')}{\omega_\kappa - \omega_n}, \quad (\text{S45})$$

where  $\psi_n$  has been normalized through  $\psi_n = \psi_n / \sqrt{\sum_j \psi_n(j)^2}$ . By combining Eqs. (S45) and (S43), we can obtain the following result

$$r_\kappa = -i\Gamma_0 \sum_{j,j',n} e^{i\omega_\kappa/c(z_{j'}+z_j)} \frac{\psi_n(j)\psi_n(j')}{\omega_\kappa - \omega_n}, \quad (\text{S46})$$

When the frequency of the photon is in resonance with the energy of an excitation state [i.e.,  $\omega_\kappa = \text{Re}(\omega_n)$ ], then the denominator only takes the value of the imaginary part of the eigenvalue  $\text{Im}(\omega_n)$ . If the eigenstate  $|\psi_n\rangle$  is a subradiant state with  $\text{Im}(\omega_n) \ll \Gamma_0$ , then reflection is mainly determined by the properties of the  $n$ th eigenstate. Hence, we can neglect the summation over the quantum number in Eq. (S46) and yield the reflection coefficient

$$r_\kappa \approx \Gamma_0 \sum_{j,j'} e^{i\omega_\kappa/c(z_{j'}+z_j)} \frac{\psi_n(j)\psi_n(j')}{\text{Im}(\omega_n)}. \quad (\text{S47})$$

Thus, reflection may give information about the localization property of subradiant states.

## S6. WINDING NUMBER OF SCATTERING TEXTURES

In this section, we show the summarized results in the Chart I of the main text. Without loss of generality, we choose the two typical sets of parameters in the topological nontrivial phase ( $\varphi \approx 1$ ,  $\theta = 0$ ) and trival phase ( $\varphi \approx 1$ ,  $\theta = \pi$ ), and calculate the winding number of scattering textures in the lower inverse band of subradiant states; see Fig. S4. The other parameters are chosen as  $g = 1$ ,  $\Gamma_0 = 0.01$ , and  $\omega_0 = 100$ . When the number of cells is not less than 4, the winding number of scattering textures is precisely quantized, either 0 or 1. No matter for topological nontrivial phase or trival phase, the winding number strongly depends on the even-odd number of the cells. For the topological nontrivial phase, the winding number is 1 for the even cell number and 0 for the odd cell number. For the trival phase, the winding number is 0 for the even cell number and 1 for the odd cell number. This is the first time that we find that the winding number of scattering textures is affected by both the topological phase of excitation and the even-odd effect of cell number.

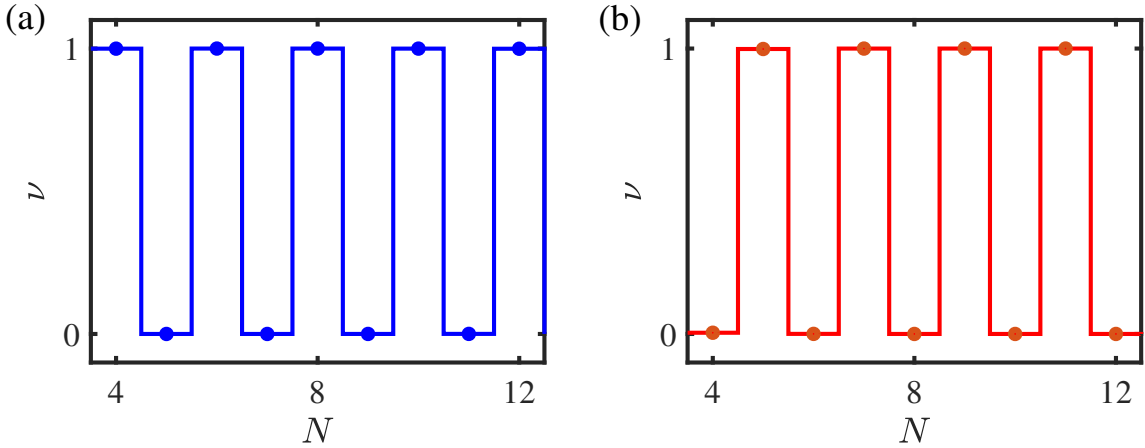


FIG. S4. Winding number of scattering texture as a function of cell number in (a) topological nontrivial phase and (b) trival phase. The parameters are chosen as  $g = 1$ ,  $\Gamma_0 = 0.01$ ,  $\omega_0 = 100$ ,  $\varphi = 1$ ,  $\theta = 0$  and  $\theta = \pi$  for topological and trival phases, respectively.

## S7. PHASE SHIFT DUE TO SUBRADIANT STATES

In this section, we numerically verify that there exists a  $\pi$  phase shift due to the subradiant states. We calculate the reflection and the phase of reflection by sweeping the inverse energy through the lower inverse energy band of the subradiant states; see Fig. S5. For the case of topological nontrivial phase (left panel of Fig. S5), there are  $(N - 1)$

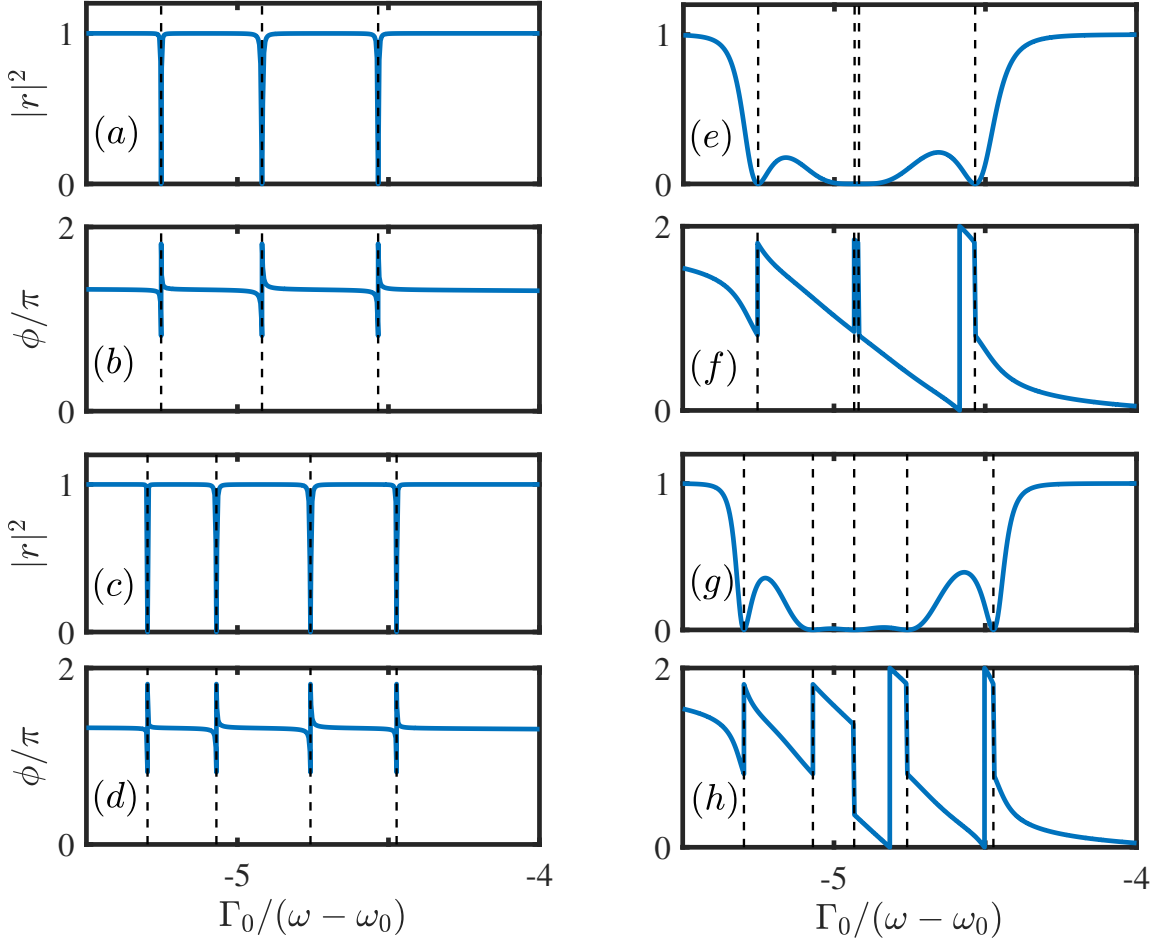


FIG. S5. Reflection and phase of reflection as functions of inverse energy. The left and right panels correspond to topological nontrivial phase ( $\varphi \approx 1$ ,  $\theta = 0$ ) and trival phase ( $\varphi \approx 1$ ,  $\theta = \pi$ ), respectively. (a, b, c, d), (e, f, g, h) show the Reflection and phase of reflection in 4 and 5 cells. The dash lines indicate the inverse energies for the dip and  $\pi$  phase shift, which are around the energies of subradiant states. The other parameters are chosen as  $g = 1$ ,  $\Gamma_0 = 0.01$  and  $\omega_0 = 100$ .

subradiant states for  $N$  cells. When the frequency of a photon is in resonance with the subradiant states, the photon becomes completely transmission, and there exist dips at the inverse energy of the subradiant states. In Figs. S5(a) and (c), the number of dips in the inverse energy band is 3 and 4, corresponding to 4 and 5 cells. We can also find that there exists  $\pi$  phase shift at the resonant points in Figs. S5(b) and (d), which are calculated with the same parameters as Figs. S5(a) and (c), respectively. For the case of the trival phase (right panel of Fig. S5), there are  $N$  subradiant states for  $N$  cells. There are 4 and 5 dips in the reflection spectrum with 4 and 5 cells; see Figs. S5(e) and (g). Because the decay rates of the subradiant states are relatively larger and comparable to the energy difference between the subradiant states, the reflection cannot simply be attributed to individual subradiant states but rather the collective effect of the nearby subradiant states. Hence, the positions of dips slightly depart from the inverse energies of individual subradiant states. However, the  $\pi$  phase shifts are also accompanied by the dips. By sweeping through the lower inverse energy band of the subradiant states, we can find that there are  $(N - 1)$  and  $N$  times of  $\pi$  phase shifts for topological nontrivial and trival phases, respectively. Since the sum of  $\pi$  phase shifts depends on both the topological phase of excitation and the even-odd number of cells, similar to the winding number of scattering textures, there should be intimate relation the  $\pi$  phase shift induced by subradiant states and the winding number.

We can attribute the winding number of scattering textures to the sum of  $\pi$  phase shifts.

---

- [1] J.-T. Shen and S. Fan, Strongly correlated two-photon transport in a one-dimensional waveguide coupled to a two-level system, *Phys. Rev. Lett.* **98**, 153003 (2007).
- [2] L. Li, C. H. Lee, and J. Gong, Impurity induced scale-free localization, *Communications Physics* **4**, 1 (2021).
- [3] Y. Ke, A. V. Poshakinskiy, C. Lee, Y. S. Kivshar, and A. N. Poddubny, Inelastic scattering of photon pairs in qubit arrays with subradiant states, *Phys. Rev. Lett.* **123**, 253601 (2019).
- [4] Y. Ke, J. Zhong, A. V. Poshakinskiy, Y. S. Kivshar, A. N. Poddubny, and C. Lee, Radiative topological biphoton states in modulated qubit arrays, *Phys. Rev. Research* **2**, 033190 (2020).